Vortices in ultrashort laser pulses

P. Hansinger · A. Dreischuh · G.G. Paulus

Abstract The propagation of optical vortices nested in broadband femtosecond laser beams was studied both numerically and experimentally. Based on the nonlinear Schrödinger equation, the dynamics of different multiple-vortex configurations with varying topological charge were modelled in self-focussing and self-defocussing Kerr media. We find a similar behavior in both cases regarding the vortex–vortex interaction. However, the collapsing background beam alters the propagation for a positive nonlinearity. Regimes of regular and possibly stable multiple filamentation were identified this way. Experiments include measurements on pairs of filaments generated in a vortex beam on an astigmatic Gaussian background with argon gas as the nonlinear medium. Spectral broadening of these filaments leads to a supercontinuum which spans from the visible range into the infrared. Recompression yields <19 fs pulses. Further optimization may lead to much better recompression.

1 Introduction

Optical vortices (OV) are singular points within the beam profile of a light beam, around which the phase varies by

P. Hansinger (✉) · G.G. Paulus
Institut für Optik und Quantenelektronik,
Friedrich-Schiller-Universität Jena, Max-Wien-Platz 1,
07743 Jena, Germany
e-mail: peter.hansinger@uni-jena.de

A. Dreischuh
Department of Quantum Electronics, Sofia University,
5, J. Bourchier Blvd., Sofia 1164, Bulgaria

G.G. Paulus
Helmholtz-Institut Jena, Helmholtzweg 4, 07743 Jena, Germany

an integer multiple m of 2π over the angular coordinate φ. m is called the topological charge of the vortex, which can be viewed as photon angular momentum. Due to the undefined phase, the intensity vanishes at the singularity point of the helical phase profile [1]. The study of OVs has received special attention in recent years not only because of their rich linear and nonlinear dynamics [2–7], but also due to a variety of potential applications including particle micro-manipulation [8], imaging [9], interferometry [10], and quantum information [11]. Particularly interesting is the case of OVs in broadband coherent continua such as ultrashort laser pulses, as those beams will allow for the study of nonlinear phenomena in various media. To date there exist several methods to create OV beams from femtosecond laser pulses: dispersionless 4f- [12–14] or 2f–2f-setups [15], double-pass grating compressors [13] or achromatic vortex lenses [16]. In addition, polychromatic OVs (and OV solitons) can also be generated by uniaxial crystals [17, 18]. Most of the early efforts in the exploration of nonlinear vortex propagation were put into the research of self-defocussing media. Dark vortex solitons were observed this way [2] and have been proposed as a method of optical-optical control [7]. Only recently the generation of white light by OV beams in a self-focussing medium has been demonstrated in CaF_2 [19]. An inherent issue of this process is the emergence of instabilities which amplify inhomogeneities in the beam profile up to the point of collapse [20, 21].

In this work we numerically model and compare the interactions of optical vortices in local self-defocusing and self-focusing Kerr nonlinear media. We seek rotational and translational rigid OV lattices which, under self-focusing conditions, can bring ordering in the multiple filamentation of the background beam and can provide the necessary refractive index modulation for off-site guiding of or-

dered probe beams. Experiments are done with a pair of filaments generated from an OV beam on an astigmatic Gaussian background, and emphasis is put on the recompressibility of the resulting white-light continuum after filamentation.

2 Theoretical results

The simulations are carried out in the framework of the time-independent $(2 + 1)$D nonlinear Schrödinger equation describing the evolution of the slowly-varying envelope:

$$i\frac{\partial A(x, y, z)}{\partial (z/L_D)} + \frac{1}{2}\Delta_T A(x, y, z)$$
$$+ \text{sign}(n_2)\frac{L_D}{L_{NL}}\big|A(x, y, z)\big|^2 A(x, y, z) = 0. \quad (1)$$

z is the longitudinal propagation coordinate, Δ_T accounts for linear diffraction, whereas the third term on the left-hand-side models the optical Kerr effect. The sign of the nonlinear coefficient is positive for self-focussing and negative for self-defocussing media. The OV beam is modeled as

$$A(x, y, z = 0) = A_0 B(x, y) \tanh\left(\frac{\sqrt{x^2 + y^2}}{r_0}\right)e^{im\varphi}, \quad (2)$$

where

$$B(x, y) = e^{-(\frac{x^2+y^2}{r_{BG}^2})^8} \quad (3)$$

describes the profile of the super-Gaussian background beam. The characteristic length scales are $L_D = kr_0^2$ (diffraction) and $L_{NL} = \frac{1}{kn_2 I}$ (Kerr effect). The equation is solved using the split-step Fourier method on a 1024×1024 grid. Parameters are chosen as $r_{BG} = 0.64 \times 512$ pix and $r_0 = 14.7$ pix. The intensity was kept identical to the one needed to form an optical vortex soliton (OVS) with unity charge ($I = I_{SOL}^{OV}$), unless noted otherwise. The calculation is stopped at $z = 5L_{NL}$ in the self-defocussing case and at $z = 2L_{NL}$ in the self-focussing case (because of beam collapse).

2.1 Two vortices with identical/alternating TC

It is known that vortices of equal TC repel each other and rotate because of nonzero net TC. In contrast, vortices of opposite TC attract each other and translate on the background beam, finally leading to annihilation of the vortices. This interaction gets stronger with decreasing distance/larger overlap between the vortex cores. We calculated the propagation for inter-vortex distances of 28 pix and 42 pix and recorded relative positions of the vortices with respect to the initial
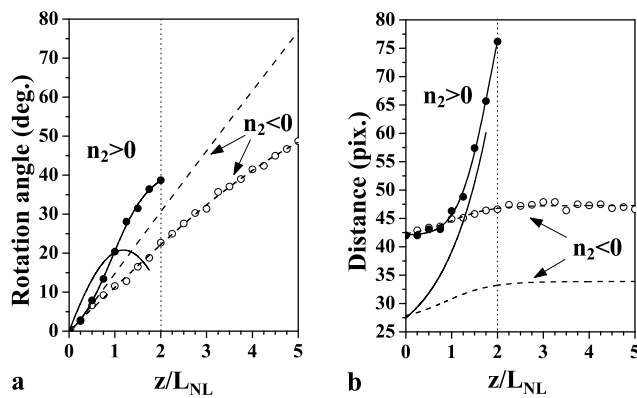
Fig. 1 Two OVs, equal TCs. Vortex pair rotation angle (**a**) and distance between the vortices (**b**) vs. nonlinear propagation length. *Open circles* and *dashed lines* refer to $n_2 < 0$, *solid circles* and *solid curves* correspond to $n_2 > 0$. Initial vortex–vortex distance 42 pix (*open/solid circles*) and 28 pix (curves with no symbols)
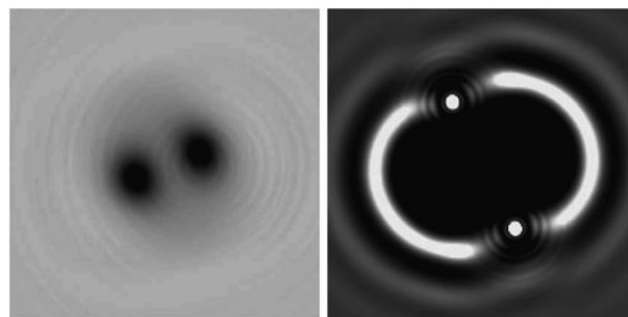

Fig. 2 Two OVs, equal TCs. OV pairs of equal TCs at $z = 2L_{NL}$ for negative (*left*) and positive Kerr nonlinearity (*right*). Initial vortex–vortex distance 42 pix. Because of the self-focusing and for better visibility the gray scale for the *right frame* is 2.5 times higher than for the *left frame*. About 3.8% of the total computational area are shown

profile. The results are shown in Figs. 1 and 2. For identical TC, we find that the fundamental behavior does not change when n_2 changes its sign. However, the interaction is enhanced in the self-focussing case, leading to faster rotation and stronger repulsion. Particularly notable is the reversal of the rotation direction for closely spaced cores. For opposite TCs, the situation is fundamentally different: In the self-defocusing case, the inter-vortex distance increases almost linearly with z as expected (Fig. 3). In the self-focussing case and for sufficiently distant vortex cores, asymmetric self-focussing peaks develop rapidly between the cores and push the vortices apart (Fig. 4). Nonlinear repulsion clearly prevails over the (linear) TC attraction, which can be seen in the increasing distance of the vortex cores. The propagation is significantly affected by self-focussing and the resulting gradients in the beam profile that interact with the vortices.
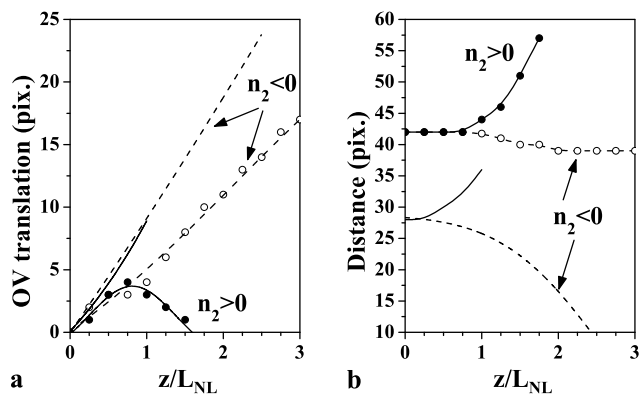
Fig. 3 Two OVs, opposite TCs. Vortex pair shift (**a**) and vortex–vortex distance (**b**) vs. nonlinear propagation length. *Open circles* and *dashed lines* refer to $n_2 < 0$, *solid circles* and *solid curves* correspond to $n_2 > 0$. Initial vortex–vortex distances 42 pix (*open/solid circles*) and 28 pix (curves with no symbols)
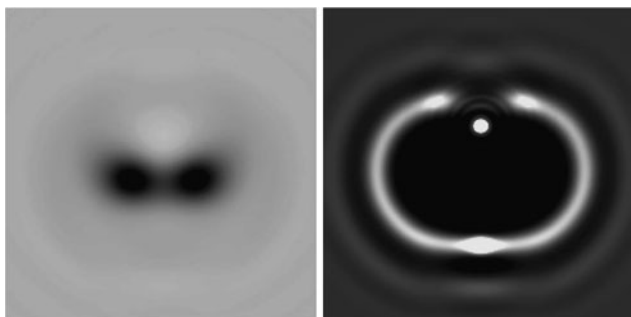

Fig. 5 Three OVs, equal TCs. Rotation angle (**a**) and distance between two of the vortices (**b**) vs. nonlinear propagation length. *Open circles* and *dashed lines* refer to $n_2 < 0$, *solid circles* and *solid curves* correspond to $n_2 > 0$. Initial vortex–vortex distances 42 pix (*open/solid circles*) and 28 pix (curves with no symbols)

Fig. 4 Two OVs, opposite TCs. OV pairs at $z = 1.75L_{NL}$ for negative (*left*) and positive Kerr nonlinearity (*right*). Initial vortex-vortex distance 42 pix. Because of the self-focusing and for better visibility the gray scale for the *right frame* is 2.5 times higher than this for the *left frame*. About 3.8% of the total computational area are shown

Fig. 6 Three OVs, equal TCs. Three OVs at $z = 1.75L_{NL}$ for negative (*left*) and positive Kerr nonlinearity (*right*). Initial vortex-vortex distances 42 pix. Because of the self-focusing and for better visibility the gray scale for the *right frame* is 2.5 times higher than this for the *left frame*. About 4.6% of the total computational area are shown

2.2 Three vortices on a line

The next situation modeled was the case of three equidistant vortices on a line, with equal or alternating TCs. The case of net zero TC with a doubly charged central vortex was also considered. We find a qualitatively similar behavior for the equal TC case compared to the two-vortex configuration (Fig. 6). However, the rotation of the linear array is slower for both $n_2 < 0$ and $n_2 > 0$. The slowing and sign reversal of the rotation can also be seen in Fig. 5.

The case of alternating TC shows a different picture: For the larger initial vortex distance of 2×42 pix, self-focussing peaks in between the cores arise and frustrate the attraction of the vortices (Fig. 7). Annihilation is therefore not observed. Due to the nonzero net TC, rotation of the linear array can also be observed and follows qualitatively the two-vortex scheme, yet with different speeds. Starting with a smaller 2×28 pix vortex array, self-focussing takes place outside the inter-vortex core region, and therefore we observe annihilation of two vortices of opposite charge (see Fig. 8). Interestingly, repulsion between the outer two cores
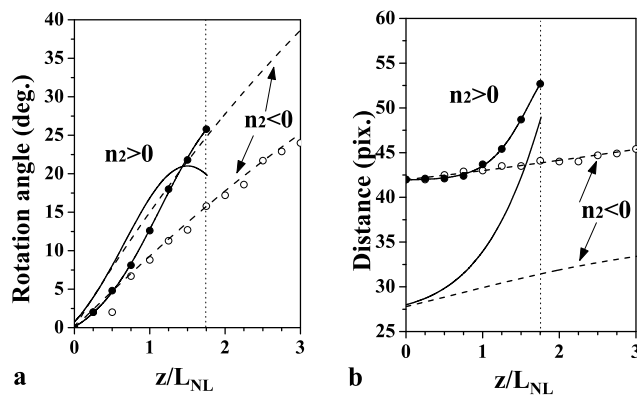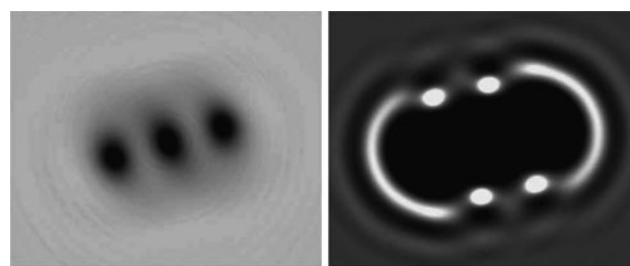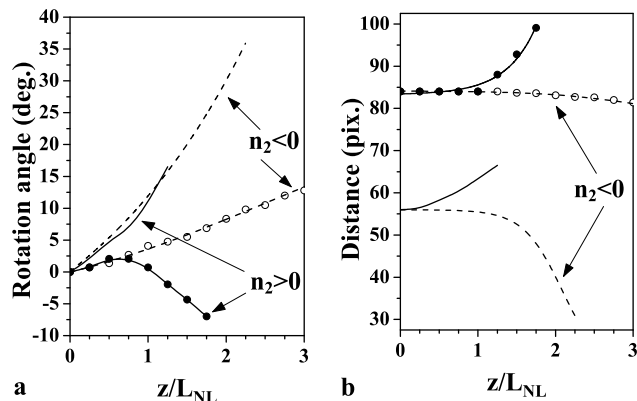

Fig. 7 Three OVs, alternating TCs. Rotation angle (**a**) and distance between the two outer vortices (**b**) vs. nonlinear propagation length. *Open circles* and *dashed lines* refer to $n_2 < 0$, *solid circles* and *solid curves* correspond to $n_2 > 0$. Initial vortex structure length 2×42 pix (*open/solid circles*) and 2×28 pix (no symbols)

is still observed. We conclude that, during propagation, instabilities lead to symmetry breaking that subsequently favors one of the outer vortices for recombination with the central one.
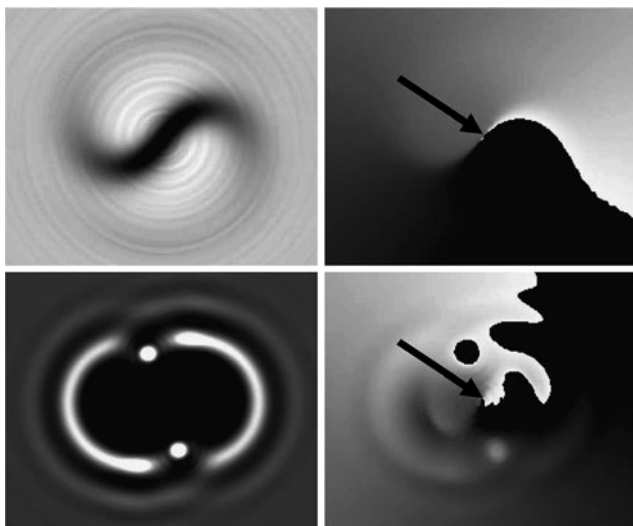
Fig. 8 Three OVs, alternating TCs. Intensity (*left*) and phase profiles (*right*) of three in-line OVs at $z = 2.5L_{NL}$ for negative (*top row*) and at $z = 1.75L_{NL}$ for positive Kerr nonlinearity (*bottom row*). Initial vortex-vortex distances 28 pix. The gray scale for the lower *left frame* is 2 times higher than this for the *upper left frame*. The *arrows* in the phase profiles indicate the cores of the vortices after the annihilation of the respective OV pairs. About 4.6% of the total computational area are shown

Fig. 9 Three OVs, central one doubly-charged. Intensity (*left*) and phase profiles (*right*) at $z = 5L_{NL}$ for negative (*top row*) and at $z = 1.5L_{NL}$ for positive Kerr nonlinearity (*bottom row*). Initial vortex–vortex distances 42 pix. The gray scale for the *lower left frame* is 2 times higher than this for the *upper left frame*. The *arrows* in the phase profiles indicate the cores of the vortices. About 4.6% of the total computational area are shown

Finally we simulated a linear vortex structure of TC $+1/-2/+1$ to investigate the influence of the central vortex charge upon propagation. The central vortex is not stable and decays into two vortices with unit charge, which strongly repel each other. For $n_2 < 0$, this leads to two pairs of vortices with opposite TC. Both pairs translate parallel to their axes on the background beam. This is also true in the self-focussing case, but here we observe annihilation of the vortex pairs at $z \approx 2L_{NL}$ (2×42 pix) and $z \approx 1.25L_{NL}$ (2×28 pix) accordingly (Fig. 9). Again, for the smaller array, the vortex-vortex interaction (namely repulsion of the central two cores) is more pronounced.

2.3 Alternating vortex lattice

Finally the results above were generalized to the case of a square lattice array of vortices with alternating TCs. First we modeled the corresponding elementary cell of four vortices located at the corners of a square. Despite strong self-focussing of the background beam, the vortex cores keep their initial positions upon propagation. Figure 10 shows the beam profile and phase after $z = 1L_{NL}$. The simulated vortex array assembled from this elementary cell consists of some 600 vortices. The intensity was raised to $I = 1.268I_{SOL}^{OV}$ to compensate for the peak reduction due to overlapping cores. Resulting beam profiles are shown in Fig. 11. In the linear propagation regime, the intensity profile develops into a basketweave-like structure. For negative n_2, the vortices in the central part of the array keep their initial positions, whereas background beam gradients and diffraction
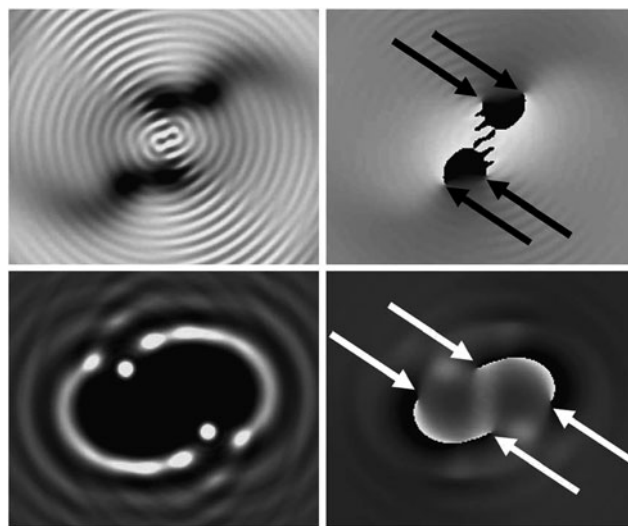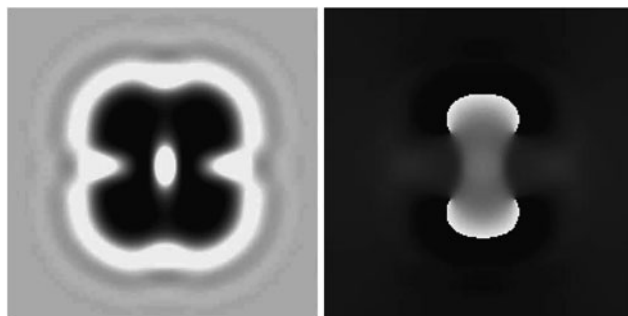

Fig. 10 Four OVs, alternating TCs. Intensity (*left*) and phase profile (*right*) at $z = 1L_{NL}$ for positive Kerr nonlinearity. Initial vortex–vortex distances 42 pix. About 3.8% of the total computational area are shown

increase the intervortex distance to 60 pix in the outer regions. In the self-focussing case, the off-site points (with regard to the vortex positions) of higher intensity undergo self-focussing and evolve into a regular array. The basketweave-like structure can still be seen in the slightly elliptical filament shapes with alternating orientation of their principal axes.

3 Experimental results

3.1 Setup

The method used to create unit TC OVs in the lab is a 16-level AR-coated spiral phase plate (SPP) optimized for 800 nm. The higher damage threshold as compared to, e.g.,
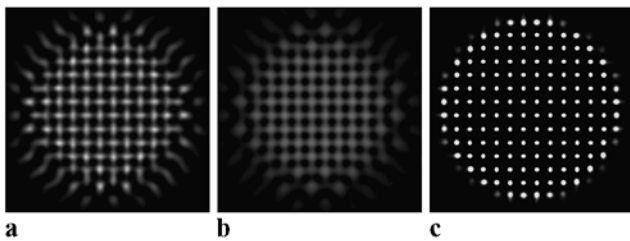
Fig. 11 Large rectangular array of OVs with a vortex–vortex distance of 42 pix. Linear evolution (**a**) and propagation in self-defocusing regime (**b**) up to $z = 5L_{NL}$. Ordered multiple filaments created off-site with respect to the vortex array is self-focusing regime (**c**). In the nonlinear regimes 40% of the total computational area are shown
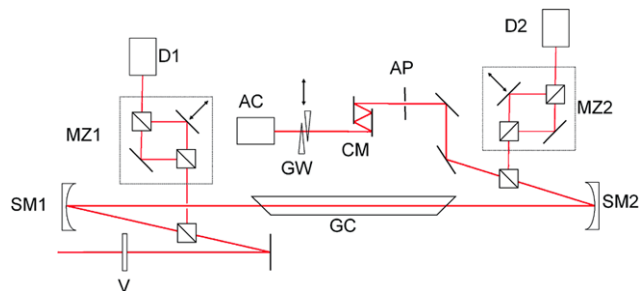

Fig. 12 Experimental setup. V: Spiral phase plate, SM1: spherical mirror $f = 2$ m, GC: gas cell, SM2: spherical mirror $f = 3$ m, MZ1/MZ2: Mach–Zehnder interferometer, D1/D2: CCD camera, AP: aperture, CM: chirped mirrors, GW: glass wedges, AC: interferometric autocorrelator

Fig. 13 Output beam profiles. Simulated linear propagation (*top left*), simulated nonlinear propagation (*top right*), measured linear propagation (*bottom left*), measured nonlinear propagation (*bottom right*). Images correspond to a position 1.5 m after the linear focus and pressures of 0.00 bar (linear case) and 1.80 bar (nonlinear case) in the gas cell respectively

an SLM allows for the usage of the higher intensities which are needed to seed one or more filaments. This SPP shows good conversion efficiency over the full bandwidth of our laser with a maximum phase difference between the outermost spectral components of <3%. Diffraction from the SPP due to the discrete structure is present but reasonably low and does not affect the vortex in the far field. Our laser is a commercial Ti:Sa CPA system, consisting of a 25-fs, 1-mJ, 4-kHz frontend (Femtolasers) and a subsequent 30-fs, 10-mJ, 1-kHz amplification stage. Either of the two output beams can be sent through the SPP and focussed with a $f = 2$ m spherical mirror into a 1.5-m long gas cell with Brewster-angled windows. The cell is filled with Argon at an adjustable pressure of 0.0–2.0 bar. The output of the gas cell is collimated by a $f = 3$ m spherical mirror and recompressed by a set of chirped mirrors. The chirp can be fine-tuned with two glass wedges, and the pulse duration is measured with an interferometric autocorrelator. Input and output spectra as well as the beam profile are recorded with two VIS-NIR spectrometers and two high-resolution 14-bit CCD cameras (Fig. 12).

3.2 Results

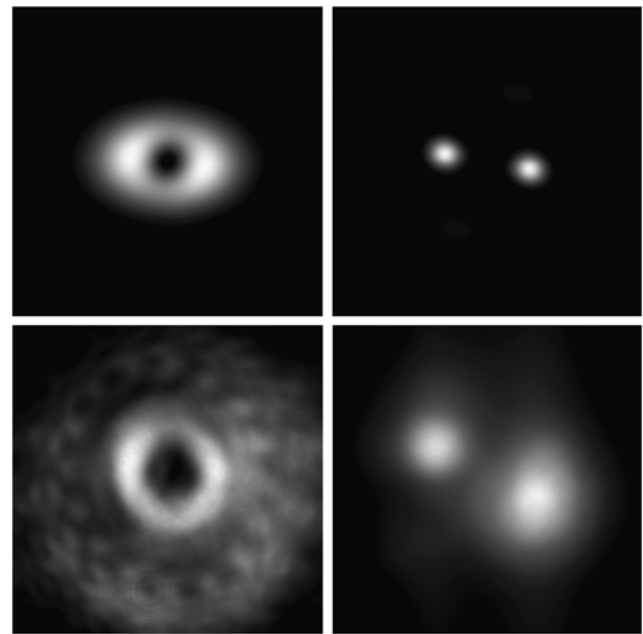Although the generated vortex beam before the gas cell shows notable diffraction, the image in the focal plane exhibits no significant distortion, and the vortex is well reproduced in the far field. Amplification of the inhomogeneities in the intensity ring through self-focussing leads to breakup of the beam into single filaments (Fig. 13). The theoretical number of these filaments scales with the peak power and the topological charge (see [20]) and never exceeds $n_{Filament} = 3$ in our experiments. Relative peak intensities (related to the maximum spectral broadening) of these filaments are levelled by adjusting the position of the SPP within the beam. Throughout the experiment, the output power of the laser is kept constant, and the nonlinearity is controlled by varying the particle density inside the gas cell via the gas pressure. The chirp of the pulse was adjusted for maximum spectral broadening with the grating compressor of the laser. Spectral broadening takes place through self- and cross-phase modulation, as well as self-steepening and the influence of the generated plasma [21]. The single-shot output profiles for different gas pressures are shown in Fig. 13. Starting from 0.00 bar, self-focussing increases until a minimum output diameter of the filaments is obtained at 1.80 bar. For higher pressures, the broadening of the spectrum increases and results in larger output beams due to stronger diffraction of the infrared components. Single filament cores are then selected with a pinhole after collimation of the output beam, and the spectrum is measured. Figure 14 shows typical output spectra for different pressures. Notable broadening sets in at 1.20 bar. At the highest

Fig. 14 Output spectra as function of pressure. Notable spectral broadening takes place above 1.20 bar. The spectral modulation at zero pressure is caused by the input window of the gas cell. Spectrometer range was limited from 500–110 nm
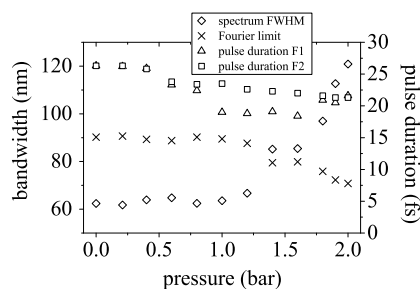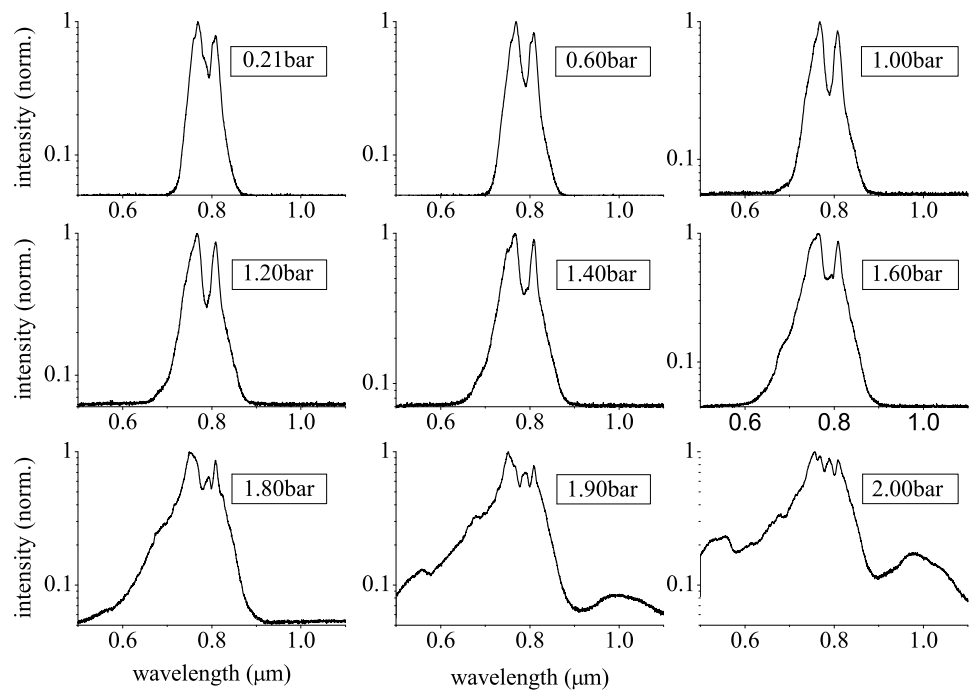
the two filaments can be explained by different peak intensities of the two parts of the pump beam. The diffracting background from the SPP has no significant influence at low pressures (linear regime) but amplifies one of the filaments in the self-focussing regime. Despite careful alignment of the SPP, the photon reservoir of the background beam acts strongly on the propagation beam. Further regularization of the propagation and control of this background is therefore necessary.

Fig. 15 Pulse compression. Spectral bandwidth (FWHM) (*diamonds*), bandwidth-limited pulse duration (*crosses*) and achieved pulse duration after compression for the two filaments (*triangles*, *squares*)

4 Conclusions

The theoretical results indicate the existence of a regime where stable structures of multiple filaments can be created. A balance between self-focussing and vortex TC interaction also seems possible since any realistic medium will undergo saturation of the nonlinearity with increasing intensity. Possible mechanisms are a quintic nonlinearity of opposite sign [22] or ionization/free electron generation that stops the beam collapse [23]. The theoretical model does not yet include temporal effects, which are expected to significantly alter the propagation, especially for short pulses [21]. Future work will include these effects.

Experiments have yielded moderate compression rates of femtosecond laser pulses using optical vortices, which can be optimized further. A key element is the recompression of the supercontinuum after the filament. Optimized chirped mirrors with higher-order dispersion compensation may prove useful here. In addition, self-compression is a

pressure measured, the FWHM bandwidth of the filament is 120 nm, which corresponds to bandwidth-limited pulse duration of 7.8 fs. The initial spectral modulation present is due to SPM in the input window. The single filaments were then recompressed by the chirped mirrors, with each mirror bounce leading to -60 fs^2 of GVD. The number of mirrors was chosen as to obtain the shortest possible pulse in the autocorrelator. The respective average pulse duration vs. pressure is shown in Fig. 15. Averaging was performed to reduce the influence of fast variations in the laser intensity and disturbance by air flow in the laboratory. The shortest pulse duration of 18.4 fs in a single filament was obtained for a pressure of 1.60 bar. For pressures beyond that, the output becomes increasingly unstable and compression was less effective. The reason for this are nonideal chirp of the input beam and the increasing importance of higher-order dispersion due to the larger bandwidth. The difference between

feasible mechanism to obtain short pulses in single filaments [24]. Whether this is also possible with vortex-lattice filaments is subject of ongoing research, as well as the coherent superposition of the individual filament beams. A single vortex provides only limited control over multiple filament propagation because of the self-focussing surrounding background beam.

References

1. J. Nye, M. Berry, Proc. R. Soc. Lond. Ser. A, Math. Phys. Sci. **336**, 165 (1974)
2. Y. Kivshar, B. Luther-Davies, Phys. Rep. **298**, 81 (1998)
3. A. Desyatnikov, Y. Kivshar, L. Torner, Prog. Opt. **47**, 291 (2005)
4. G. Swartzlander Jr, C. Law, Phys. Rev. Lett. **69**, 2503 (1992)
5. Z. Chen, M. Shih, M. Segev, D. Wilson, R. Muller, P. Maker, Opt. Lett. **22**, 1751 (1997)
6. A. Carlsson, J. Malmberg, D. Anderson, M. Lisak, E. Ostrovskaya, T. Alexander, Y. Kivshar, Opt. Lett. **25**, 660 (2000)
7. C. Law, X. Zhang, G. Swartzlander et al., Opt. Lett. **25**, 55 (2000)
8. D. Grier, Nature **424**, 810 (2003)
9. G. Foo, D. Palacios, G. Swartzlander Jr, Opt. Lett. **30**, 3308 (2005)
10. S. Fürhapter, A. Jesacher, S. Bernet, M. Ritsch-Marte, Opt. Express **13**, 689 (2005)
11. G. Molina-Terriza, J. Torres, L. Torner, Nat. Phys. **3**, 305 (2007)
12. K. Bezuhanov, A. Dreischuh, G. Paulus, M. Schätzel, H. Walther, Opt. Lett. **29**, 1942 (2004)
13. K. Bezuhanov, A. Dreischuh, G. Paulus, M. Schätzel, H. Walther, D. Neshev, W. Królikowski, Y. Kivshar, JOSA B **23**, 26 (2006)
14. I. Zeylikovich, H. Sztul, V. Kartazaev, T. Le, R. Alfano, Opt. Lett. **32**, 2025 (2007)
15. I. Mariyenko, J. Strohaber, C. Uiterwaal, Opt. Express **13**, 7599 (2005)
16. G. Swartzlander Jr, Opt. Lett. **31**, 2042 (2006)
17. D. Neshev, A. Dreischuh, V. Shvedov, A. Desyatnikov, W. Krolikowski, Y. Kivshar, Opt. Lett. **33**, 1851 (2008)
18. A. Voylar, V. Shvedov, T. Fadeyeva, A. Desyatnikov, D. Neshev, W. Krolikowski, Y. Kivshar, Opt. Express **14**, 3724 (2006)
19. D. Neshev, A. Dreischuh, G. Maleshkov, M. Samoc, Y. Kivshar, Opt. Express **18**, 18368 (2010)
20. L. Vuong, T. Grow, A. Ishaaya, A. Gaeta, G. Hooft, E. Eliel, G. Fibich, Phys. Rev. Lett. **96**, 133901 (2006)
21. A. Couairon, A. Mysyrowicz, Phys. Rep. **441**, 47 (2007)
22. M. Quiroga-Teixeiro, H. Michinel, JOSA B **14**, 2004 (1997)
23. S. Tzortzakis, B. Prade, M. Franco, A. Mysyrowicz, Opt. Commun. **181**, 123 (2000)
24. C. Hauri, W. Kornelis, F. Helbing, A. Heinrich, A. Couairon, A. Mysyrowicz, J. Biegert, U. Keller, Appl. Phys. B **79**, 673 (2004)